Concentrator photovoltaic module architectures with capabilities for capture and conversion of full global solar radiation

Kyu-Tae Lee[a,b,1], Yuan Yao[c,1], Junwen He[c,1], Brent Fisher[d], Xing Sheng[e], Matthew Lumb[f,g], Lu Xu[c], Mikayla A. Anderson[c], David Scheiman[g], Seungyong Han[a,b], Yongseon Kang[a,b], Abdurrahman Gumus[h], Rabab R. Bahabry[h], Jung Woo Lee[a,b,i,j], Ungyu Paik[i,j], Noah D. Bronstein[k], A. Paul Alivisatos[k,l,m,n], Matthew Meitl[d], Scott Burroughs[d], Muhammad Mustafa Hussain[h], Jeong Chul Lee[a,b,2], Ralph G. Nuzzo[a,b,c,2], and John A. Rogers[a,b,c,2]

[a]Department of Materials Science and Engineering, University of Illinois at Urbana–Champaign, Urbana, IL 61801; [b]Frederick Seitz Materials Research Laboratory, University of Illinois at Urbana–Champaign, Urbana, IL 61801; [c]Department of Chemistry, University of Illinois at Urbana–Champaign, Urbana, IL 61801; [d]Semprius, Durham, NC 27713; [e]Department of Electronic Engineering, Tsinghua University, Beijing, China 100084; [f]The George Washington University, Washington, DC 20037; [g]US Naval Research Laboratory, Washington, DC 20375; [h]Integrated Nanotechnology Lab, Computer, Electrical and Mathematical Sciences and Engineering Division, King Abdullah University of Science and Technology, Thuwal, Saudi Arabia; [i]Department of Materials Science and Engineering, Hanyang University, Seoul 133-791, Republic of Korea; [j]Department of Energy Engineering, Hanyang University, Seoul 133-791, Republic of Korea; [k]Department of Chemistry, University of California, Berkeley, CA 94720; [l]Department of Materials Science and Engineering, University of California, Berkeley, CA 94720; [m]Kavli Energy NanoScience Institute, University of California, Berkeley, CA 94720; and [n]Materials Science Division, Lawrence Berkeley National Laboratory, Berkeley, CA 94720

Contributed by John A. Rogers, October 21, 2016 (sent for review September 7, 2016; reviewed by Yi Cui and Gary P. Wiederrecht)

Emerging classes of concentrator photovoltaic (CPV) modules reach efficiencies that are far greater than those of even the highest performance flat-plate PV technologies, with architectures that have the potential to provide the lowest cost of energy in locations with high direct normal irradiance (DNI). A disadvantage is their inability to effectively use diffuse sunlight, thereby constraining widespread geographic deployment and limiting performance even under the most favorable DNI conditions. This study introduces a module design that integrates capabilities in flat-plate PV directly with the most sophisticated CPV technologies, for capture of both direct and diffuse sunlight, thereby achieving efficiency in PV conversion of the global solar radiation. Specific examples of this scheme exploit commodity silicon (Si) cells integrated with two different CPV module designs, where they capture light that is not efficiently directed by the concentrator optics onto large-scale arrays of miniature multijunction (MJ) solar cells that use advanced III–V semiconductor technologies. In this CPV$^+$ scheme ("+" denotes the addition of diffuse collector), the Si and MJ cells operate independently on indirect and direct solar radiation, respectively. On-sun experimental studies of CPV$^+$ modules at latitudes of 35.9886° N (Durham, NC), 40.1125° N (Bondville, IL), and 38.9072° N (Washington, DC) show improvements in absolute module efficiencies of between 1.02% and 8.45% over values obtained using otherwise similar CPV modules, depending on weather conditions. These concepts have the potential to expand the geographic reach and improve the cost-effectiveness of the highest efficiency forms of PV power generation.

photovoltaics | multijunction solar cells | concentration optics | diffuse light capture

The levelized cost of electricity (LCOE) is a primary metric that defines the economic competitiveness of photovoltaic (PV) approaches to electrical power generation (1). As the performance of the highest efficiency single-junction flat-plate PV modules begins to reach theoretical limits, research toward cost reductions in such technologies shifts from performance to topics related to materials utilization and manufacturing (2–5). By contrast, the efficiencies of multijunction (MJ) solar cells based on III–V compound semiconductors continue to improve steadily, at a rate of ∼1% per year over the last 15 y, due largely to progress in epitaxial growth processes, mechanical stacking techniques, and microassembly methods for adding junctions that further maximize light absorption and minimize carrier thermalization losses (6–20). Record MJ cell efficiencies now approach ∼46.0%, with realistic pathways to the 50% milestone (5). For economic deployment, however, the sophistication and associated costs of these cells demand the use of lenses, curved mirrors, or other forms of optics in conjunction with a mechanical tracker to geometrically concentrate incident direct sunlight in a manner that maximizes cell utilization (21, 22). One commercial technology of interest uses a two-stage optical concentrating system that consists of an array of aspheric primary lenses and ball lenses interfaced to arrays of ultrathin, triple-junction (3J) III–V cells with submillimeter lateral dimensions formed by lithographic processes and epitaxial liftoff (23–25).

Significance

Concentrator photovoltaic (CPV) systems, wherein light focuses onto multijunction solar cells, offer the highest efficiencies in converting sunlight to electricity. The performance is intrinsically limited, however, by an inability to capture diffuse illumination, due to narrow acceptance angles of the concentrator optics. Here we demonstrate concepts where flat-plate solar cells mount onto the backplanes of the most sophisticated CPV modules to yield an additive contribution to the overall output. Outdoor testing results with two different hybrid module designs demonstrate absolute gains in average daily efficiencies of between 1.02% and 8.45% depending on weather conditions. The findings suggest pathways to significant improvements in the efficiencies, with economics that could potentially expand their deployment to a wide range of geographic locations.

Author contributions: K.-T.L., Y.Y., J.H., X.S., J.C.L., R.G.N., and J.A.R. designed research; K.-T.L., Y.Y., J.H., B.F., M.L., L.X., M.A.A., D.S., S.H., Y.K., A.G., R.R.B., J.W.L., U.P., N.D.B., A.P.A., M.M., S.B., M.M.H., J.C.L., R.G.N., and J.A.R. performed research; K.-T.L., Y.Y., J.H., B.F., J.C.L., R.G.N., and J.A.R. analyzed data; and K.-T.L., Y.Y., J.H., R.G.N., and J.A.R. wrote the paper.

Reviewers: Y.C., Stanford University; and G.P.W., Argonne National Laboratory.

Conflict of interest statement: B.F., M.M., S.B., R.G.N., and J.A.R. are affiliated with Semprius, a company that is pursuing commercial, grid-scale photovoltaic technologies that form a starting point for the advanced embodiments described and studied in this paper. Semprius does not, however, have any active programs toward commercialization of these embodiments. The authors declare that B.F., M.M., S.B., R.G.N., and J.A.R. are involved in Semprius, a company that has commercialized certain classes of concentrator photovoltaic technologies.

[1]K.-T.L., Y.Y., and J.H. contributed equally to this work.

[2]To whom correspondence may be addressed. Email: jcleegm@illinois.edu, r-nuzzo@illinois.edu, or jrogers@illinois.edu.

This article contains supporting information online at www.pnas.org/lookup/suppl/doi:10.1073/pnas.1617391113/-/DCSupplemental.

Here, transfer printing enables high-volume manufacturing and assembly of cells with these small dimensions (26–32). The ball lenses, as secondary optics, improve manufacturing tolerances, produce uniform irradiation profiles on the cells by correcting for chromatic aberration, and expand the acceptance angle to nearly ±1° even at concentration ratios of >1,000 (22). The compact sizes and weights of the resulting high-concentrator PV (HCPV) modules facilitate transport and installation and enable use of mechanical trackers with cost-effective designs. Production systems exhibit efficiencies of 35.5% at concentration ratios >1,000× under Concentrator Standard Test Conditions (CSTC).

Terrestrial use of these, and other, types of HCPV technologies is most economically attractive in geographic locations with high levels of direct normal irradiance (DNI) (e.g., >6 kWh/m^2/d). Typical sites in the United States include California, Arizona, and New Mexico (33). Limitations follow from the inability to use nondirect (i.e., diffuse) sunlight due to narrow acceptance angles of the concentrating optics, as dictated by the étendue conservation law (e.g., with a passive concentrator operating at a concentration ratio of 1,000, the acceptance angle is theoretically limited to 1.8°) (34). Even in locations such as Tucson, AZ (17% diffuse) and Daggett, CA (20% diffuse) that have exceptionally high DNI, the enhancements associated with capture and conversion of diffuse illumination can be significant. In other locations such as San Francisco (29.6% diffuse) and Portland, OR (39.2% diffuse), operation under diffuse light becomes even more essential to the economics. Engineering solutions to this challenge have the potential to expand the application of concentrator systems to areas where they have previously been uncompetitive (35, 36). *SI Appendix*, Fig. S1 presents estimates for the absolute increases in efficiency that can be expected in these locations (35). As a perspective on the significance, calculations using detailed balance predict that the efficiency enhancements enabled by adding a diffuse collector with an optimized bandgap can exceed those provided by a replacement of 4J cells with 5J alternatives under standard AM 1.5G spectrum (10% diffuse) (*SI Appendix*, Fig. S2). The ability to use diffuse sunlight also makes CPV less susceptible to soiling issues, as the scattered (by soiling) direct beam rays, which are not concentrated onto the high-efficiency MJ cells (ranges from 2% to 10% depending on locations and weather conditions; *SI Appendix*, Fig. S3), can be captured by the diffuse collectors. As a first attempt to capture diffuse light, a recent report introduced a prototype minimodule device built on a conventional CPV platform through the addition of silicon (Si) cells with arrays of circular holes to allow passage of focused light onto underlying MJ cells (36). This demonstration, however, involved concentration ratios (<500×) that are too low to be economically viable, and standard cells and single-stage optical components that pose significant challenges in thermal management, efficient/accurate tracking, and manufacturing tolerances. The two advanced CPV technologies examined here avoid these and other key limitations, thereby providing the basis for a realistic, competitive approach to PV power generation.

The work reported here examines advanced modes of implementation and detailed analysis in the context of the most advanced commercially available HCPV module, designed for utility-scale power generation in solar farms, as described above, and of a previously unpublished, ultrathin design, configured for use on rooftops and in space applications. Specifically, the following results experimentally and theoretically examine schemes that incorporate capabilities in diffuse light capture into these two types of module architectures. The version that uses the HCPV technology outlined above exploits laser-cut strips of conventional Si cells, without machined holes, mounted in a form-fitting manner onto the module backplanes. These systems offer economically viable concentration ratios, (>1,000×) with advanced microscale cells for improved thermal management, and dual-stage optics for efficient/accurate tracking and manufacturing tolerances. (In the following, we refer to this module architecture as HCPV$^+$-DS, where "+" refers to capabilities in diffuse light capture and DS to the dual-stage optics). The other architecture employs a compact design optimized for diffuse light capture, where MJ cells on a transparent substrate stack directly onto an unmodified commodity Si cell. These components couple to an overlying thin plano-convex (PCX) lens array, enabling an exceptionally low-profile module (<5 mm in total thickness) suitable for deployment in space-restricted areas (e.g., rooftops) or in applications where weight is a primary concern (e.g., portable systems, or space applications). (In the following, we refer to this module architecture as CPV$^+$-LP, where the LP refers to low-profile optics and the absence of H refers to the modest concentration ratios.) Compared with conventional designs, the CPV$^+$-LP architecture offers additional cost advantages because its ultracompact size and lightweight design significantly reduce both installation/transportation expenses and the steel required for the mechanical tracker.

The economic rationale for both of these designs rests on the fact that ∼80% of the cost of energy from flat-plate PV technology comes from non–cell-related balance-of-module and balance-of-system (BOS) cost associated with land, transport, installation, and maintenance (i.e., the turnkey cost in Q4-2015 of a utility-scale plant with tracking is \$1.54/W$_{dc}$ and the cost of the Si cells is \$0.33/W) (2, 37). As a result, the addition of the Si cells to an otherwise well-designed CPV platform can represent an incremental cost, justified by the improved performance and consistency of output. Specifically, at current market prices, the cost of the Si cells (i.e., without enclosure, package, inverter, BOS cost, etc.) in a conventional flat-plate PV system corresponds to ∼15% of the LCOE for that system (1, 37). Assuming that the CPV technology used in this work is economically competitive with Si flat plate in regions of moderate to high DNI (38), the cost for adding Si cells to CPV is approximately only 7.5% of the LCOE, because the output per unit area of a Si module is roughly one-half that for a corresponding CPV module. The economic case for the CPV$^+$ concept follows from comparison of the marginal cost of adding the Si (7.5%) to the benefit in terms of additional energy generated. Experimental results reported here suggest that the addition of Si cells to CPV modules increases the overall energy production by roughly 10% even in regions of the United States with the most abundant direct solar radiation resources (diffuse component ∼20%, assuming the Si cell efficiency is ∼50% of the CPV module), thereby supporting the potential for an overall reduction in the LCOE. Current trends in reductions in the costs of Si cells and increases in the efficiencies of III–V cells could make such CPV$^+$ architectures even more attractive in the future.

The CPV$^+$ concept also yields significant increases in power per unit area, relevant for all applications: from deployment in regions of high DNI where ∼20% of the solar resource is in the form of diffuse light, to markets with constrained rooftop space, and to geographic domains with modest DNI. Outdoor field testing of HCPV$^+$-DS and CPV$^+$-LP modules, as described in detail subsequently, shows absolute increases in efficiencies of between 1.02% and 8.45% at a latitude of 35.9886° N (Durham, NC), 1.97–6.06% at a latitude of 40.1125° N (Bondville, IL), and 5.20% at a latitude of 38.9072° N (Washington, DC) in typical weather conditions in the spring, summer, and fall months. An additional advantage of these systems is that the large numbers of cells in the platforms provide flexibility in matching their electrical outputs to yield standardized two-terminal module interfaces (39).

Results and Discussion

Fig. 1*A* shows a schematic illustration of the working principles of the HCPV$^+$-DS design. Two-stage optics [i.e., a primary high concentration (HC), inward-facing array of PCX lenses on a

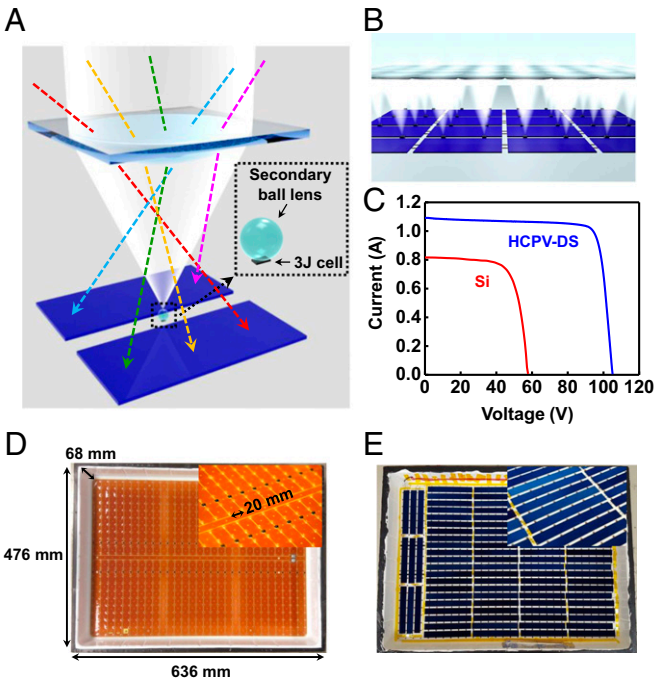

Fig. 1. Schematic diagrams, images, and performance characteristics of an HCPV system that exploits dual-stage concentrator optics, with microscale 3J cells to capture direct irradiation and Si solar cells to capture diffuse irradiation, which we refer to as an HCPV^{+}-DS module. (*A*) Schematic illustration of a unit cell in the module that highlights the two-stage optics design (1,000× concentration) and the interconnected array of the Si cells (blue rectangles) on the backplane in regions between the 3J cells with integrated ball lenses (*Inset*), yielding a system that captures both direct (gray/blue shaded region) and diffuse (colored dashed lines to show representative trajectories) solar radiation. (*B*) Schematic view at the module level (a collection of 32 unit cells). (*C*) Current (*I*)–voltage (*V*) curves for the HCPV-DS module (measured under CSTC from a flash test) and the interconnected array of Si cells (measured on sun outdoors). Photographs and magnified views as insets showing (*D*) the standard HCPV-DS module panel backplane consisting of an array of the 3J cells coupled with ball lenses and (*E*) the hybrid HCPV^{+}-DS module which includes the Si cells.

front panel, and a collection of secondary ball lenses mounted directly onto the 3J cells) concentrate direct sunlight (1,000×) onto the 3J cells (InGaP/GaAs/InGaAsNSb, 1.9 eV/1.4 eV/1.0 eV). Adjacent Si cells collect diffuse sunlight, which cannot be captured effectively by the concentrating optics. These Si cells are laser cut from larger, commercially available cells (interdigitated back contact; A3000, SunPower Corp.) to sizes that fit the areas between the 3J cells, as illustrated in Fig. 1*B*. Representative *I-V* characteristics from the unmodified HCPV module measured under flash test conditions (1,000 W·m^{-2}, T_{cell} = 25 °C) and from an interconnected array of laser-cut Si cells under sun exposure outdoors (950 W·m^{-2}, measured without the primary lens) appear in Fig. 1*C*. The HCPV module shows an open-circuit voltage (V_{oc}) of 105.2 V, a short-circuit current (I_{sc}) of 1.09 A, and an energy conversion efficiency (η) of 34.0%. The array of Si cells has a V_{oc} of 57.8 V, an I_{sc} of 0.816 A, and an η of 18.5%. Photographs of the module backplane before and after integrating the Si cells are in Fig. 1 *D* and *E*: The complete HCPV^{+}-DS module consists of 660 3J cells (600 μm × 600 μm, intercell spacing: 20 mm) and 93 Si cells (16.1 mm × 127 mm) with a full HCPV aperture area of 0.264 m^2 and total Si cell area of 0.190 m^2. These components mount in a white powder-coated steel enclosure (636 mm × 476 mm × 68 mm) with a polymer-encapsulated copper backplane. The Si cells, interconnected in series without bypass diodes, cover 72% of the available backplane area. These components bond onto a white plastic insulating substrate for mechanical support and for ease of integration into the overall housing.

The CPV^{+}-LP embodiment provides complementary capabilities and illustrates the versatility of the overall concepts. Here, an array of 3J cells mount on a transparent substrate with a form factor (~100 mm × 100 mm) designed to match that of commodity Si cells, without modification (Maxeon, SunPower Corp., η = 20% under 1 sun). Stacking these two subsystems and integrating a corresponding set of single-stage low-concentration (LC) optics yields a complete module in which direct sunlight focuses onto the array of microcells while the diffuse light strikes the unmodified, underlying Si cell as illustrated in Fig. 2*A*. In an example shown here, the optics consist of an array of glass LC outward-facing PCX aspheres (18×) with thickness of 2.5 mm and focal length of 1 mm, in a hexagonal array with 3-mm pitch. The entire stack, as shown in Fig. 2*B*, provides for a low-profile module with a thickness that is less than 5 mm and a Si cell coverage that approaches ~100% (96% after taking the shading by the 3J cells into account). Characteristic *I-V* performance curves for the array of 3J cells and the Si cell appear in Fig. 2*C*. These data correspond to simultaneous measurements from a single module on a tracker during an outdoor field test in Washington, DC under partly cloudy skies on March 3, 2016

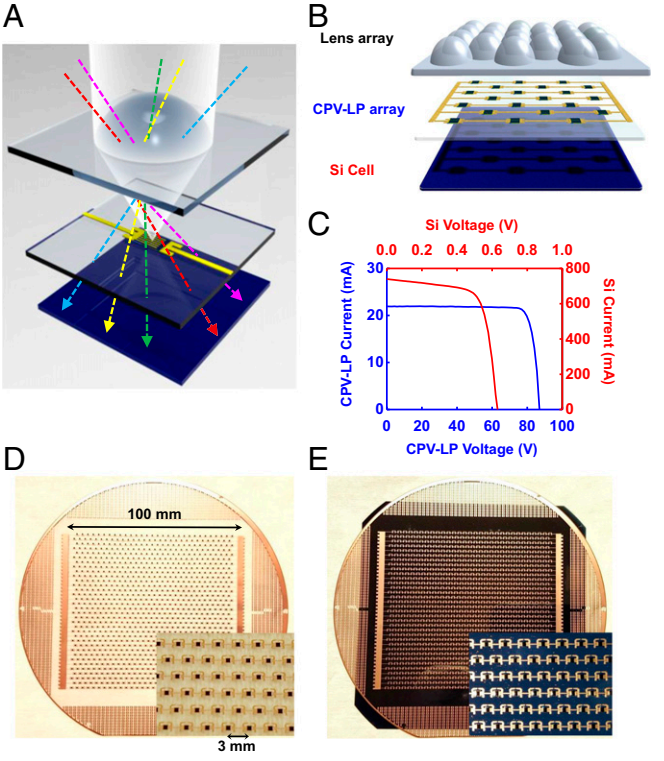

Fig. 2. Schematic representations, photographs, and electrical performance of a low-profile CPV system that exploits single-stage concentrator optics, with microscale 3J cells to capture direct irradiation and Si solar cells to capture diffuse irradiation, which we refer to as a CPV^{+}-LP. (*A*) Schematic illustration of a unit cell in the CPV-LP^{+} module that includes an array of 3J cells on a transparent substrate located between a corresponding array of focusing lenses above and a single Si cell below. This system captures both direct (concentrated onto the 3J cells) and diffuse (illuminating the Si cell) solar irradiation. (*B*) Exploded view schematic illustration of the CPV-LP^{+} module design. (*C*) Current (*I*)–voltage (*V*) characteristics of the CPV-LP module and the Si cell (measured outdoors; blue for CPV; red for Si). (*D* and *E*) Photographs and zoom-in insets of a completed module of this type (i.e., CPV^{+}-LP) before and after the underlying Si cell integration.

[global normal irradiance (GNI) = 1,053.0 W m^{-2}; DNI = 682.2 W m^{-2}]. The 3J cell array operates at high voltage (V_{oc} = 87.0 V) and low current (I_{sc} = 21.9 mA), due to an electrical configuration of 34 parallel-connected strings of 30 series connected cells, each of which generates over 3 V under CSTC. The Si cell yields correspondingly higher currents (I_{sc} = 740 mA) and lower voltages (V_{oc} = 0.631 V). Fig. 2 *D* and *E* present optical images of the assembled device before and after integrating with the underlying Si cell without a top LC outward-facing PCX lens array. Fig. 2 *D* and *E* (*Inset*) images show a cell arrangement and an interconnection scheme.

Diffuse solar radiation has a wide angular spread and follows a broad range of beam trajectories through the concentrating optics. As the angular distribution of diffuse irradiance can vary with meteorological conditions, the calculations presented here assume a Lambertian distribution. For the front lens arrays in both module architectures, the transmittance of light incident at various incidence angles (θ) can be simulated by ray tracing (LightTools). Results for the primary, inward-facing HC PCX lens array in the HCPV-DS module (f/# = focal length/lens diameter = 3) appear in Fig. 3*A*. At incidence angles greater than 30°, the transmittance suffers from total internal reflection (TIR) within the array, as highlighted by calculations that do not consider Fresnel reflection losses (black curves in Fig. 3*A*; see *SI Appendix*, Fig. S4 for ray path illustrations). These losses (both TIR and Fresnel) continue to increase as the incidence angle increases. Similar trends appear in simulations for the outward-facing LC PCX lens array for the CPV-LP module (f/# = 2.3; *SI Appendix*, Fig. S5).

The averaged transmittance of diffuse light through a PCX lens unit in either module design is also related to its focusing power. As shown by the simulated results in Fig. 3*B* and *SI Appendix*, Fig. S5, larger values of f/# (i.e., a smaller focusing power) lead to higher transmittance due to reduced TIR losses within the PCX lens, whereas the Fresnel losses (difference between the red and black curves) remain nearly constant. The f/# also influences the irradiance distribution on the focal plane, as shown by the calculated results in Fig. 3*C* and *SI Appendix*, Fig. S5. The spatial uniformity of these irradiance profiles can be defined by their root-mean-square deviation (RMSD), according to

$$\mathrm{RMSD} = \sqrt{\frac{1}{n-1}\sum_{i=1}^{n}\left(\frac{I_i}{I_{avg}}-1\right)^2}, \qquad [1]$$

where I_i is the irradiance of a sampling pixel at some location and I_{avg} is the overall averaged irradiance on the panel backplane. As presented in Fig. 3*B* and *SI Appendix*, Fig. S5, the RMSD reaches negligible values when the f/# is larger than 2. The PCX lens arrays in both module architectures fulfill this criterion.

Similar ray-tracing methods can simulate the distribution of diffuse irradiance that forms on both types of module backplanes after passage through the PCX lens array. This quantity is important for efficient capture and conversion by the Si cells. Calculations, again assuming Lambertian angular distribution for the incoming diffuse light, for the HCPV$^+$-DS module reveal these distributions for three different sidewall reflectivity conditions (mirror, diffuse, and absorbing), as shown in Fig. 4. Reflecting sidewalls (i.e., 100% specular reflection) generate the most even backplane diffuse light distribution (RMSD = 0.0059; Fig. 4*A*), equivalent to the case of an infinite lens array where projections of diffuse light through multiple single lenses (*SI Appendix*, Fig. S6) overlap to create uniform irradiance. The overall optical efficiency (η_{op}) for passage of diffuse light through the primary lens array and arrival at the backplane is 76%, restricted by losses from Fresnel reflections (11%) and limited acceptance angles for photons at large incidence angles due to TIR within the primary lens array (13%). For the case of a 10% diffuse light component in the incident solar illumination,

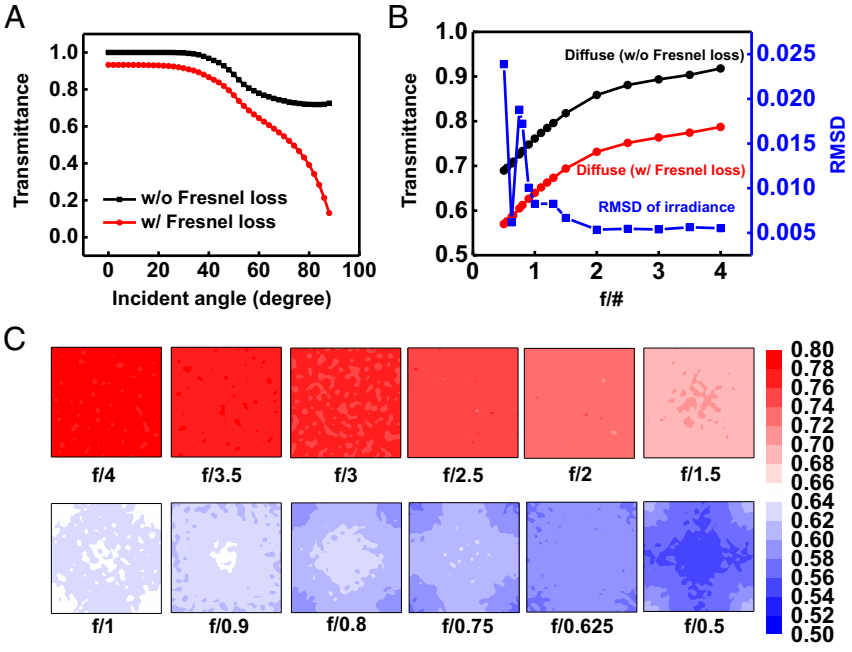

Fig. 3. Simulation results for transmittance, irradiance uniformity, and irradiance distribution associated with passage of diffuse light (Lambertian) through inward-facing HC plano-convex lens arrays in the HCPV$^+$-DS systems. (*A*) Simulated averaged transmittance of the lens array as a function of the incident angle of light measured relative to the normal direction. (*B*) Dependence of the transmittance of diffuse sunlight and diffuse irradiance uniformity on the f/# (focal length divided by lens diameter). The calculations involve ray tracing at a wavelength of 550 nm for the case of an infinite lens array, with the lens profile optimized as conic surfaces for convergent focal points. (*C*) Normalized irradiance distribution under an infinite lens array for different f/#, with a sampling area equivalent to that of a single lens unit: higher f/# leads to a higher irradiance uniformity.

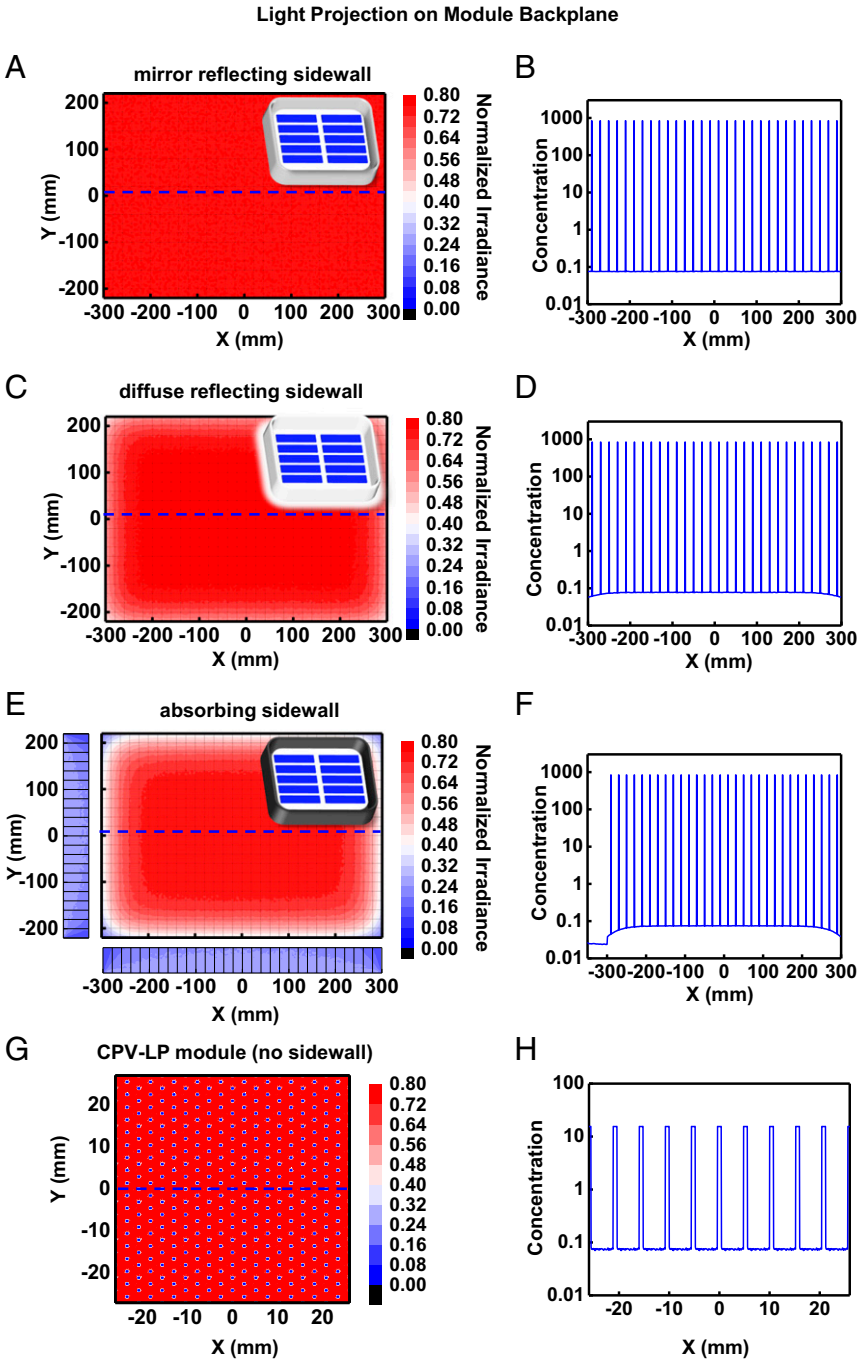

Fig. 4. Simulated diffuse irradiance profiles and total concentration ratios for the HCPV^{+}-DS panel backplane with different sidewall conditions, and for the CPV^{+}-LP module. (*A* and *B*) Mirror reflecting sidewall; (*C* and *D*) diffuse reflecting sidewall; (*E* and *F*) absorbing sidewall. The concentration ratio is calculated along the blue dashed line across the panel backplane as shown on the diffuse irradiance profiles. (*G* and *H*) Simulated diffuse irradiance distribution and total concentration ratios of a part of the CPV^{+}-LP module.

the total normalized irradiance in the form of concentration level (relative to one-sun illumination) can be calculated along a dashed line (Fig. 4*A*) that overlaps with the locations of the 3J cells, as plotted in Fig. 4*B*. The sharp peaks and flat regions represent the concentrated light and diffuse radiation, respectively. The module housings involve sidewalls covered by glossy white powder coat paint, with a scattering reflective condition closer to a Lambertian diffusive surface. The simulation results for this case are in Fig. 4 *C* and *D*. Although the diffuse irradiance distribution shows some variation near the edges of the module, leading to RMSD = 0.11 over the whole panel backplane, the uniformity remains excellent in the central region (16 × 24 lens units, RMSD = 0.016). The overall optical efficiency (η_{op}) for the diffuse irradiance in this case (diffuse sidewall) is 73%. The global efficiency gain (η_{gain}) of the HCPV^{+}-DS module can be estimated by multiplying η_{op} with the Si cell efficiency (η_{Si} = 18.5%), the fraction of the solar illumination that is diffuse (f_{diff}), and the Si cell areal coverage ratio on the panel backplane ($f_A = 0.72$). When $f_{diff} = 20\%$ (e.g., a typical sunny day in New Mexico, California, and Nevada), the expected η_{gain} from

the array of the Si cells is $f_{diff} \times \eta_{op} \times \eta_{Si} \times f_A = 1.9\%$. In complete overcast conditions ($f_{diff} = 100\%$), the estimated efficiency gain from the Si cells reaches 9.7% (assuming η_{Si} remains the same under the cloudy sky spectra). An unmodified HCPV system ceases to function under such circumstances. Further improvements are possible through the addition of Si cells on the sidewalls to reach $\eta_{op} = 76\%$. Such schemes involve, however, additional costs and they significantly increase nonuniformities in the irradiance distribution on the sidewalls and backplane (The RMSD of irradiance profile on the backplane is 0.18, Fig. 4*E*). Furthermore, the irradiance on the sidewall is only ~1/3 of that of the center of the backplane (Fig. 4*F*), which would result in a voltage drop in the Si cells that may not be fully compensated by the gain in optical efficiency.

Corresponding results for the CPV$^+$-LP system appear in Fig. 4 *G* and *H*. Here, η_{op} is 75.6%, mainly limited by optical losses from the top lens array, following considerations that are similar to those associated with the primary optic in the HCPV$^+$-DS design. For this type of module ($\eta_{op} = 75.6\%$, $\eta_{Si} = 20\%$, $f_A = 0.96$), the expected η_{gain} is 2.9% and 14.5% on sunny ($f_{diff} = 20\%$) and overcast ($f_{diff} = 100\%$) days, respectively, both of which exceed values estimated for the HCPV$^+$-DS architecture due to the improved Si cell coverage.

Outdoor testing of HCPV$^+$-DS modules on a two-axis solar tracker located in Durham, NC reveals their performance under realistic operational conditions. Separate measurements collected approximately once per minute yield values for the power output from the 3J and the Si cells. A pyranometer (LiCor) and normal incidence pyrheliometer (Eppley Lab) located on a nearby tracker record the GNI and DNI. Representative data (GNI, DNI along with the power density from the HCPV-DS module, the Si cells, and the summed values, corresponding to the total output of the HCPV$^+$-DS system) under three typical weather conditions (i.e., sunny, partly sunny, and cloudy) are in Fig. 5 *A–C* (representative outdoor *I-V* curves for both CPV and Si components can be found in *SI Appendix*, Fig. S7). Fig. 5*D* and Table 1 summarize the diffuse component [i.e., (GNI-DNI)/GNI] and efficiency data against GNI (calculated over the entire

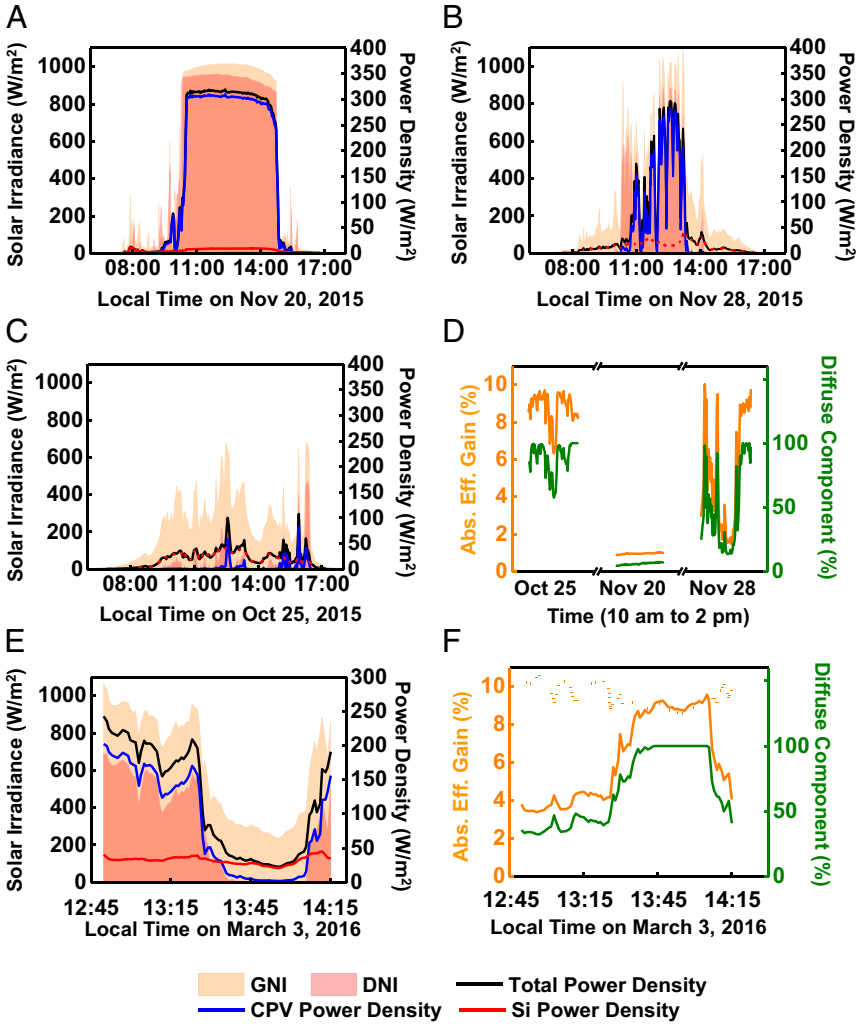

Fig. 5. Real-time outdoor testing results of GNI, DNI, and power density generated by Si (red line), CPV (blue line), and CPV$^+$ (black line). (*A*) HCPV$^+$-DS module on a sunny day (November 20, 2015) in Durham, NC from 0600 to 1800 hours. (*B*) HCPV$^+$-DS module on a partly sunny day (November 28, 2015) in Durham, NC from 0600 to 1800 hours. (*C*) HCPV$^+$-DS module on a cloudy day (October 25, 2015) in Durham, NC from 0600 to 1800 hours. (*D*) Measured real-time diffuse component of the solar spectra (green line) and absolute efficiency gain (orange line) contributed by the interconnected array of Si cells of the HCPV$^+$-DS module under different weather conditions (October 25, November 20, and November 28, 2015 in Durham, NC from 1000 to 1400 hours). (*E*) CPV$^+$-LP module on a partly sunny day (March 3, 2016) in Washington, DC from 1245 to 1415 hours. (*F*) Measured real-time diffuse component of the solar spectra (green line) and absolute efficiency gain (orange line) contributed by the Si diffuse collector of the CPV$^+$-LP module under partly sunny skies on March 3, 2016 in Washington, DC.

Table 1. Summary of measured PV characteristics of Si, CPV, and CPV$^+$ modules on different weather conditions

Condition	Date	Diffuse component, %	CPV$^+$ efficiency, %	CPV efficiency, %	Si efficiency, %
Sunny	20 November 2015	7.64	30.5	29.5	1.02
Partly sunny	28 November 2015	43.5	21.2	16.9	4.36
Cloudy	25 October 2015	84.4	10.2	1.73	8.45
Partly sunny	3 March 2016	54.3	19.0	13.8	5.20

module area) extracted from these measurements (similar data extracted from outdoor testing in Bondville, IL are presented in *SI Appendix*, Fig. S8). For the case of the sunny day (November 20, 2015, Fig. 5*A*), the DNI is over 90% and is stable (red shaded area, ~900 W/m^2) throughout the day. Here, the HCPV-DS power density (blue curve) peaks at 309.4 W/m^2 (12:19 PM) and reaches an average global efficiency ($\eta_{HCPV\text{-}DS}$) of 29.5% between 11:00 AM and 4:00 PM (note that the efficiency against the DNI is 31.9% here). The Si cells provide an added power density of 9.57 W/m^2 at the same time (red curve), which translates to an averaged absolute global efficiency gain of 1.02% when the averaged diffuse component is 7.64%, to enable $\eta_{HCPV^+\text{-}DS} = 30.5\%$ (global). On the partly sunny day (November 28, 2015, Fig. 5*B*), the DNI remains relatively high (~450 W/m^2 on average) although with strong transient variations due to clouds. The result is a peak HCPV-DS power density of 280.7 W/m^2 at 12:36 PM (DNI = 884 W/m^2) and averaged $\eta_{HCPV\text{-}DS} = 16.9\%$ (global; 29.8% against DNI). The Si cells (peak power density 43.6 W/m^2 at 1:13 PM) add 4.36% to the averaged global efficiency due to the increased diffuse illumination ($f_{diffuse}$= 43.5%), thereby yielding averaged $\eta_{HCPV^+\text{-}DS} = 21.2\%$ (global). The total power density from the HCPV$^+$-DS here peaks at 12:36 PM with a value of 296.5 W/m^2. By contrast, under cloudy conditions (October 25, 2015, Fig. 5*C*), $\eta_{HCPV\text{-}DS}$ (global) drops to 1.73%. Here, when the diffuse component is 84.4%, the Si cells produce a peak power density of 43.1 W/m^2 at 12:28 PM, and add 8.45% to the averaged global efficiency, to enable $\eta_{HCPV^+\text{-}DS} = 10.2\%$ (global). As expected, the data in Fig. 5*D* show that the absolute efficiency gain provided by the Si cells follows the trend of the diffuse component of incident radiation, with average cell efficiencies (calculated using only the area of the Si cells) of 18.4% (sunny, November 20) and 13.9% (partly sunny, November 28 and cloudy, October 25) against diffuse irradiance. The latter value matches predictions by optical simulation ($\eta_{op} \times \eta_{Si} = 0.73 \times 0.185 = 13.5\%$). The former exceeds simulation, likely because the Si cell can generate additional power from DNI scattered from intersections between lens arrays and/or imperfections in the lens surfaces (*SI Appendix*, Fig. S9).

Outdoor field test measurements with a CPV$^+$-LP module in Washington, DC on a partly sunny day (March 3, 2016) provide operational insights similar to those described above. The measured DNI and GNI, together with the power density generated by the CPV$^+$-LP module, appear in Fig. 5*E*. As with the HCPV$^+$-DS system, the maximum power generated by the 3J cell array follows the DNI profile whereas the output power from the Si cell remains fairly constant, following the trend of the diffuse irradiance (i.e., GNI-DNI). The efficiency of the 3J cell array measured in the integrated module (i.e., with optical losses from the lens array) against DNI is ~30%; that of the Si cell relative to the diffuse irradiance is ~10% (dashed orange lines in Fig. 5*F*). This Si efficiency includes effects of shading losses associated with the grid interconnects and the 3J cells as well as reflection losses associated with the concentration optics and the glass support for the 3J cell array. Compared with the previously described design, the glass support represents an additional source of loss, partly compensated by the improved coverage of the Si cell (nearly 100%), such that a similar level of averaged global efficiency gain (5.20%) relative to the averaged diffuse component (54.3%) results, as shown in Fig. 5*F*. The averaged efficiency of a CPV-LP module against GNI is 13.8%, whereas the CPV$^+$-LP system reaches 19.0% on this particular day. The data, as provided in *SI Appendix*, Fig. S9, indicate a linear relationship between the output power from the Si cells and the diffuse irradiance (GNI-DNI). Interestingly, the data from the Si cell are more tightly correlated with diffuse power at low levels of DNI (<300 W/m^2, black points) than at high levels (red points). This observation again suggests that the DNI lost by scattering from the lens array intersections and imperfections on the lens surfaces is recycled by the Si cell, similar to the effects described previously for the HCPV$^+$-DS modules (*SI Appendix*, Fig. S9).

For both types of CPV$^+$ modules, the low per-area cost of energy from Si cells makes them attractive for use on the module backplane as diffuse light collectors. Emerging alternatives based on perovskites, organics, epitaxial lift-off III–Vs, each with the additional possibility of use in advanced luminescent concentration

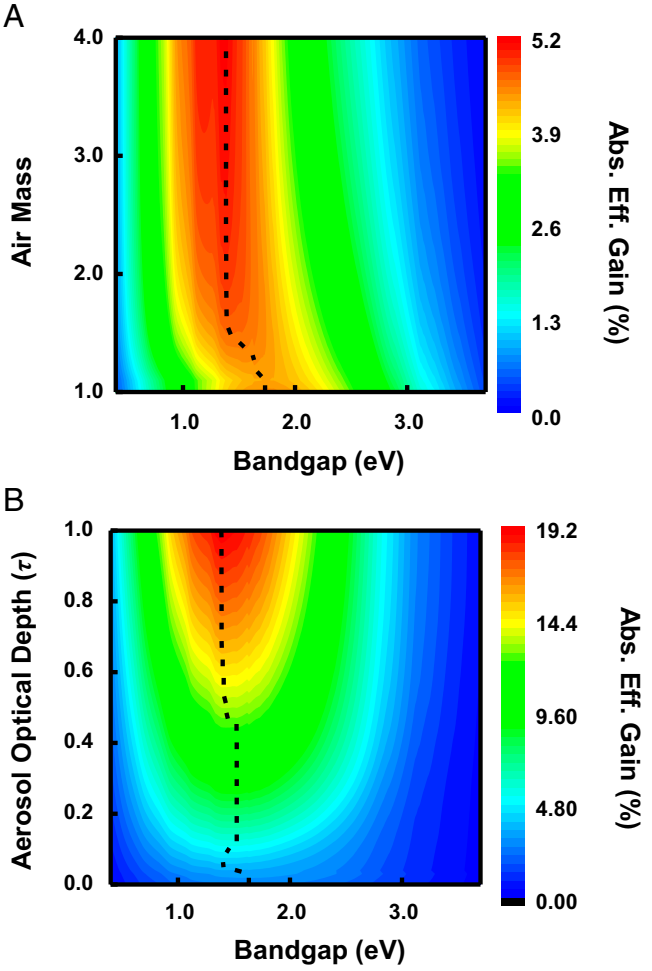

Fig. 6. Detailed balance limit of the absolute efficiency gain from diffuse light capture as a function of (*A*) air mass number and cell bandgap (τ = 0.08); (*B*) aerosol optical depth and cell bandgap (AM = 1.5).

schemes (31, 40–45), may also be considered. The bandgaps, in particular, are important. Fig. 6*A* presents the detailed balance limit for the absolute efficiency gain from diffuse light capture as a function of the cell bandgap and the air mass value, calculated based on the simulation package SMARTS (46, 47). At AM 1.5, with panel tilting angle tracking the sun, rather than a fixed 37° tilt angle used for the standard ASTM G173-03 reference spectrum (see *SI Appendix*, Fig. S10 for comparison), the absolute efficiency gain from diffuse light capture (i.e., the difference between the tilted GNI and DNI) peaks at a bandgap of 1.41 eV, which is different from the values (1.14 and 1.34 eV) optimized for the full spectrum conversion (3). This difference follows from the increased weight of the diffuse solar spectrum in the visible band compared with the full solar spectrum (*SI Appendix*, Fig. S11). The maximal efficiency gain (4.6% at 1.41 eV, with a diffuse component of 13%) is ∼0.5% higher than that predicted for Si (4.1% at 1.11 eV). As the atmosphere becomes thicker (i.e., higher AM value), the achievable efficiency gain tends to increase slightly due to the increased diffuse component, with the optimum bandgap shifting to a smaller values due to spectral variation. An ∼5% gain in efficiency is theoretically possible under thick air mass numbers (e.g., AM = 4). Increases in atmospheric turbidity, either in the form of soil dust or air pollution, lead to further increases in the diffuse component. Fig. 6*B* shows the detailed balance limit for the efficiency gain from diffuse light capture as a function of single-junction bandgap and the aerosol optical depth (τ) under AM 1.5 condition. In "clean air" (τ = 0.1) 5.0% absolute efficiency gain is expected at a bandgap of 1.37–1.56 eV, whereas in "smoky/foggy air" (τ = 0.8) 17.1% absolute efficiency boost is possible with a bandgap of 1.37–1.44 eV. Such simulations suggest value in custom backplane cell designs that optimizes the cell bandgap for different terrestrial and climate conditions.

In addition to the careful selection of cell bandgaps for diffuse light utilization, several other strategies can improve the efficiencies of the two CPV$^+$ modules introduced here. The performance of the CPV$^+$-LP system can be enhanced by: (*i*) mitigating reflection losses from lens surfaces by introducing full spectrum antireflection (AR) coatings with broad acceptance angles, with the potential for increasing the optical efficiency by 8% for direct light (i.e., 4% at each interface) and from 76% to 88% for diffuse light; (*ii*) reducing the reflections losses from the transparent substrate that supports the arrays of 3J cells, by adding the AR layer on top and an index matching liquid underneath to fill the air gap between the substrate and the Si cell, with the potential to improve the optical efficiency by 8% for diffuse light; (*iii*) increasing the concentration ratio to hundreds of suns, with the potential to increase the efficiency for direct sunlight by ∼3%; and (*iv*) incorporating world-record MJ cells (∼46% efficiency), with the potential to increase the efficiency for direct light by 9%. Extrapolations based on implementing all of these enhancements combined with the use of cells with optimized bandgap for diffuse light [GaAs ∼ 1.4 eV, optimized for AM = 1.5, η = 28.8% (5)], suggest that the global efficiency for the CPV$^+$-LP module measured on a partly sunny day (54.3% diffuse) like the one in Table 1 can be improved from 19.0% to 28.8%, whereas on a sunny day (10% diffuse), projected global efficiency can be improved from 28.9% to 35.2%. These improved efficiency values for the CPV$^+$-LP systems are comparable to, and can even exceed, world-record flat-plate modules formed by epitaxial growth [InGaP/GaAs dual junction from Alta Devices, η = 31.6% (5)].

For the HCPV$^+$-DS system, besides (*i*) using the AR coatings on lens surfaces (8% enhancement for direct light, 19% for diffuse light) and (*ii*) using the world-record MJ cells (9% enhancement for direct light) as mentioned earlier, the efficiency can also benefit from (*iii*) increasing the Si cell coverage on the backplane from 72% to nearly 100%. The collective impact of changes (*i*)–(*iii*), together with use of cells that have optimized bandgaps (GaAs ∼ 1.4 eV, η = 28.8%) could improve the module efficiencies reported in Table 1 from 30.5% to 36.6% (for sunny days) and from 21.2% to 30.8% (for partly sunny days).

For both CPV$^+$ module designs, these enhancements correspond to significant gains in annual average efficiency at various geographic locations in the United States (see the Future Innovations chart in *SI Appendix*, Fig. S1) In high DNI regions such as Tucson [with an annual diffuse radiation component ($f_{\mathrm{diff,avg}}$) of 17.0%)] and Daggett ($f_{\mathrm{diff,avg}}$ = 20.2%), the yearly average absolute increases in efficiency ($\Delta\eta_{\mathrm{diff,avg}}$) by adding the diffuse collector are 3.8% and 4.6%, respectively, whereas in medium DNI regions with more frequent overcast conditions such as San Francisco ($f_{\mathrm{diff,avg}}$ = 29.6%) and Portland ($f_{\mathrm{diff,avg}}$ = 39.2%), $\Delta\eta_{\mathrm{diff,avg}}$ reaches 6.7% and 8.8%, respectively. Data from installation in these and others regions of the world may yield data useful for detailed LCOE analyses in future work.

Conclusions

In summary, this paper demonstrates schemes by which advanced CPV module technologies can be readily converted into systems capable of capturing and converting both direct and diffuse solar radiation, with potentially important consequences on the cost of energy for photovoltaics. Outdoor testing results in Durham, NC, in Bondville, IL, and in Washington, DC indicate absolute increases in daily averaged module efficiencies between 1.02% and 8.45%, measured against GNI solar radiation, depending on weather conditions. Exploiting improved AR coatings on the concentrating optics and glass surfaces and implementing optimized bandgaps for the flat-plate PV materials offer near-term potential for further significant improvements in the performance characteristics. Furthermore, because these module architectures are independent of the MJ cell designs, immediate improvements in module efficiencies may be possible by leveraging future advances in MJ cell technology. The overall results suggest promising routes toward high-efficiency PV platforms, suitable wide geographic deployment.

ACKNOWLEDGMENTS. This work is part of the "Light-Material Interactions in Energy Conversion" Energy Frontier Research Center (to K.-T.L., Y.Y., J.H., X.S., L.X., M.A.A., N.D.B., A.P.A., R.G.N., and J.A.R.) funded by the US Department of Energy, Office of Science, Office of Basic Energy Sciences under Award DE-SC0001293. The work presented here was funded in part by the Advanced Research Projects Agency-Energy, US Department of Energy, under Award DE-AR0000624. J.W.L. and U.P. are supported by the Global Research Laboratory Program (K20704000003TA050000310) through the National Research Foundation of Korea funded by the Ministry of Science. A.G., R.R.B., and M.M.H. are supported by the King Abdullah University of Science and Technology Technology Transfer Office under Award GEN/1/4014-01-01. X.S. acknowledges support from National Natural Science Foundation of China (Project 51602172).

1. Branker K, Pathak MJM, Pearce JM (2011) A review of solar photovoltaic levelized cost of electricity. *Renew Sustain Energy Rev* 15(9):4470–4482.
2. Luque A, Hegedus S (2011) *Handbook of Photovoltaic Science and Engineering* (Wiley, Chichester, UK).
3. Shockley W, Queisser HJ (1961) Detailed balance limit of efficiency of p-n junction solar cells. *J Appl Phys* 32(3):510–519.
4. Polman A, Atwater HA (2012) Photonic design principles for ultrahigh-efficiency photovoltaics. *Nat Mater* 11(3):174–177.
5. Green MA, Emery K, Hishikawa Y, Warta W, Dunlop ED (2016) Solar cell efficiency tables (version 48). *Prog Photovolt Res Appl* 24(7):905–913.
6. Luque A (2011) Will we exceed 50% efficiency in photovoltaics? *J Appl Phys* 110:031301.
7. Derkacs D, Jones-Albertus R, Suarez F, Fidaner O (2012) Lattice-matched multijunction solar cells employing a 1 eV GaInNAsSb bottom cell. *J Photon Energy* 2:021805.
8. King RR, et al. (2007) 40% efficient metamorphic GaInP/GaInAs/Ge multijunction solar cells. *Appl Phys Lett* 90:183516.
9. Geisz JF, et al. (2007) High-efficiency GaInP/GaAs/InGaAs triple-junction solar cells grown inverted with a metamorphic bottom junction. *Appl Phys Lett* 91:023502.
10. King RR, et al. (2009) Band-gap-engineered architectures for high-efficiency multijunction concentrator solar cells. *The 24th European Photovoltaic Solar Energy Conference and Exhibition* (WIP-Renewable Energies, Hamburg, Germany), pp 55–61.

11. Wojtczuk S, et al. (2011) 42% 500X bi-facial growth concentrator cells. *AIP Conf Proc* 1407:9–12.
12. Sasaki K, et al. (2013) Development of InGaP/GaAs/InGaAs inverted triple junction concentrator solar cells. *AIP Conf Proc* 1556:22–25.
13. Sheng X, et al. (2014) Printing-based assembly of quadruple-junction four-terminal microscale solar cells and their use in high-efficiency modules. *Nat Mater* 13(6):593–598.
14. Tanabe K, Watanabe K, Arakawa Y (2012) III-V/Si hybrid photonic devices by direct fusion bonding. *Sci Rep* 2:349.
15. Zhao L, Flamand G, Poortmans J (2010) Recent progress and spectral robustness study for mechanically stacked multi-junction solar cells. *AIP Conf Proc* 1277:284–289.
16. Dimroth F, et al. (2014) Wafer bonded four-junction GaInP/GaAs/GaInAsP/GaInAs concentrator solar cells with 44.7% efficiency. *Prog Photovolt Res Appl* 22:277–282.
17. Derendorf K, et al. (2013) Fabrication of GaInP/GaAs//Si solar cells by surface activated direct wafer bonding. *IEEE J Photovolt* 3:1423–1428.
18. Takamoto T, et al. (1997) InGaP/GaAs and InGaAs mechanically-stacked triple-junction solar cells. *The 26th IEEE Photovoltaic Specialists Conference* (IEEE, Anaheim, CA), pp 1031–1034.
19. Gee JM, Virshup GF (1988) A 31% efficient GaAs/silicon mechanically stacked, multijunction concentrator solar cell. *The 20th IEEE Photovoltaic Specialists Conference* (IEEE, Las Vegas, NV), 1:754–758.
20. Fraas LM, et al. (1990) Over 35% efficient GaAs/GaSb stacked concentrator cell assemblies for terrestrial applications. *The 21st IEEE Photovoltaic Specialists Conference* (IEEE, Kissimmee, FL), Vol 1, pp 190–195.
21. Chong K-K, Lau S-L, Yew T-K, Tan PC-L (2013) Design and development in optics of concentrator photovoltaic system. *Renew Sustain Energy Rev* 19:598–612.
22. Menard E, et al. (2011) Optics development for micro-cell based CPV modules. *Proc SPIE* 8108:810805.
23. Ghosal K, Burroughs S, Heuser K, Setz D, Garralaga-Rojas E (2013) Performance results from micro-cell based high concentration photovoltaic research development and demonstration systems. *Prog Photovolt Res Appl* 21(6):1370–1376.
24. Ghosal K, et al. (2014) Semprius field results and progress in system development. *IEEE J Photovolt* 4(2):703–708.
25. Kurtz S, et al. (2015) Key parameters in determining energy generated by CPV modules. *Prog Photovolt Res Appl* 23(10):1250–1259.
26. Carlson A, Bowen AM, Huang Y, Nuzzo RG, Rogers JA (2012) Transfer printing techniques for materials assembly and micro/nanodevice fabrication. *Adv Mater* 24(39):5284–5318.
27. Burroughs S, et al. (2010) A new approach for a low cost CPV module design utilizing micro-transfer printing technology. *AIP Conf Proc* 1277(1):163–166.
28. Bower CA, Menard E, Garrou PE (2008) Transfer printing: An approach for massively parallel assembly of microscale devices. *58th Electronic Components and Technology Conference, 2008, ECTC 2008* (IEEE, Lake Buena Vista, FL), pp 1105–1109.
29. Furman B, et al. (2010) A high concentration photovoltaic module utilizing micro-transfer printing and surface mount technology. *Photovoltaic Specialists Conference (PVSC), 2010 35th IEEE* (IEEE, Honolulu), pp 000475–000480.
30. Yoon J, et al. (2010) GaAs photovoltaics and optoelectronics using releasable multilayer epitaxial assemblies. *Nature* 465(7296):329–333.
31. Yoon J, et al. (2011) Flexible concentrator photovoltaics based on microscale silicon solar cells embedded in luminescent waveguides. *Nat Commun* 2:343.
32. Yao Y, Brueckner E, Li L, Nuzzo R (2013) Fabrication and assembly of ultrathin high-efficiency silicon solar microcells integrating electrical passivation and anti-reflection coatings. *Energy Environ Sci* 6(10):3071–3079.
33. Denholm P, et al. (2012) The potential role of concentrating solar power in enabling high renewables scenarios in the United States. *Technical Report* (National Renewable Energy Laboratory, Golden, CO), pp TP-6A20-56294.
34. Hernández M, et al. (2007) The XR nonimaging photovoltaic concentrator. *Proceedings of SPIE, Nonimaging Optics and Efficient Illumination Systems IV* (SPIE, San Diego), Vol 6670, pp 667005–667010.
35. Marion W, Wilcox S (1994) *Solar Radiation Data Manual for Flat-Plate And Concentrating Collectors* (National Renewable Energy Laboratory, Golden, CO), pp 1–252.
36. Yamada N, Okamoto K (2014) Experimental measurements of a prototype high concentration Fresnel lens CPV module for the harvesting of diffuse solar radiation. *Opt Express* 22(Suppl 1):A28–A34.
37. Anonymous (2015) Solar Market Insight *2015:Q4* (Solar Energy Industries Association, Boston).
38. Kost C, et al. (2013) *Levelized Cost of Electricity Renewable Energy Technologies Study* (Fraunhofer ISE, Freiburg, Germany).
39. Menard E, et al. (2011) Multi-physics circuit network performance model for CPV modules/systems. *Photovoltaic Specialists Conference (PVSC), 2011 37th IEEE* (IEEE, Seattle), pp 002268–002272.
40. Bronstein ND, et al. (2014) Luminescent solar concentration with semiconductor nanorods and transfer-printed micro-silicon solar cells. *ACS Nano* 8(1):44–53.
41. Sheng X, et al. (2013) Doubling the power output of bifacial thin-film GaAs solar cells by embedding them in luminescent waveguides. *Adv Energy Mater* 3(8):991–996.
42. Sheng X, et al. (2013) Enhanced ultraviolet responses in thin-film InGaP solar cells by down-shifting. *Phys Chem Chem Phys* 15(47):20434–20437.
43. Bronstein ND, et al. (2015) Quantum dot luminescent concentrator cavity exhibiting 30-fold concentration. *ACS Photonics* 2(11):1576–1583.
44. Xu L, et al. (2016) Enhanced photon collection in luminescent solar concentrators with distributed Bragg reflectors. *ACS Photonics* 3(2):278–285.
45. Boriskina SV, et al. (2016) Roadmap on optical energy conversion. *J Opt* 18(7):073004.
46. Gueymard C (1995) *SMARTS2: A Simple Model of the Atmospheric Radiative Transfer of Sunshine: Algorithms and Performance Assessment* (Florida Solar Energy Center, Cocoa, FL), pp 1–78.
47. Gueymard CA (2001) Parameterized transmittance model for direct beam and circumsolar spectral irradiance. *Sol Energy* 71(5):325–346.

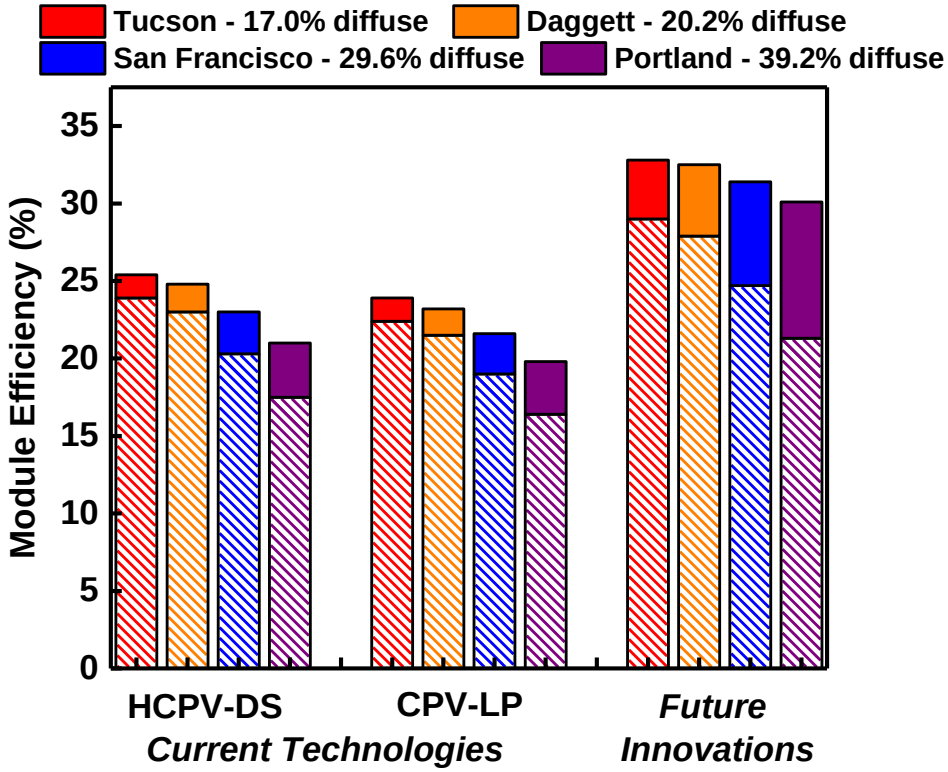

Figure S1: Estimated CPV and CPV^{+} module efficiency in different U.S. locations based on their yearly diffuse components. The current technologies tab assumes efficiencies achieved in this work (HCPV-DS module: 32.0%, CPV-LP module: 30.0%, Si cell: 18.5%), while future innovations tab uses improved PV efficiencies (CPV module: 38.9%, GaAs cell: 28.8%) along with reduced module optical losses due to implementations of AR coatings

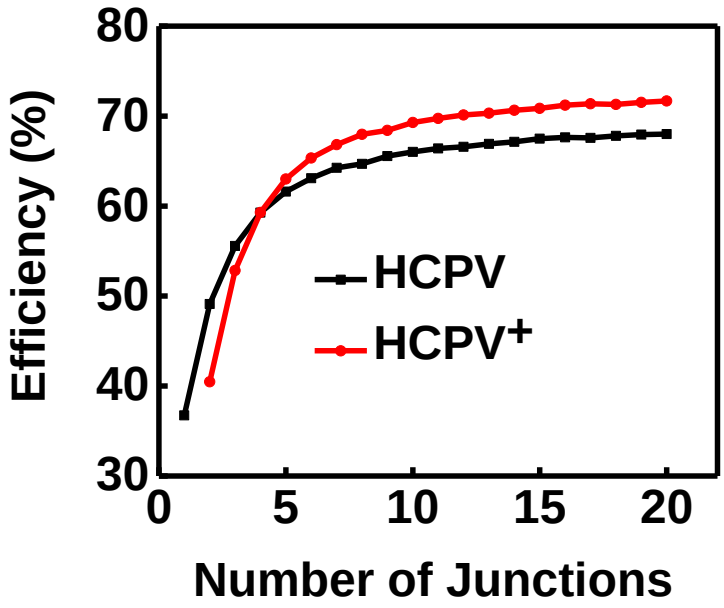

Figure S2: Detailed balance efficiency comparison between conventional HCPV MJ cells (n junctions for direct sunlight) and CPV^{+} configuration (n-1 junctions for direct sunlight and 1 junction for diffuse sunlight) at 1000 X concentration under ASTM G173-03 reference spectrum. When n=5, a combination of 4J CPV module and a diffuse collector would result in a higher efficiency than a 5J CPV system.

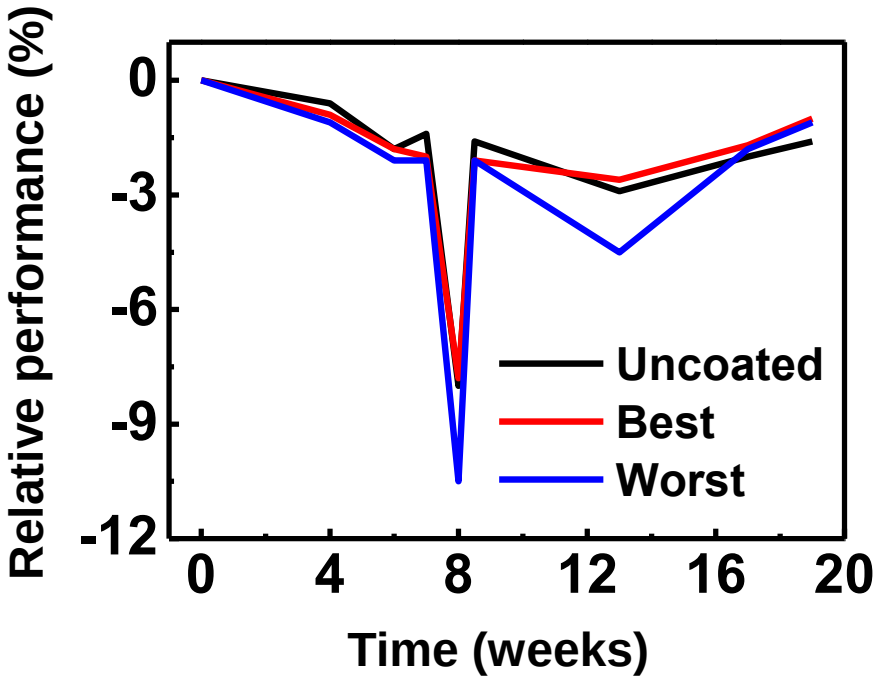

Figure S3: Relative performance of Semprius commercial modules with different experimental coatings evaluated for anti-soiling performance. The spike at 8 weeks corresponds to the extreme pine pollen season in Durham, NC. The recovery was induced by rain cleaning, without manual intervention.

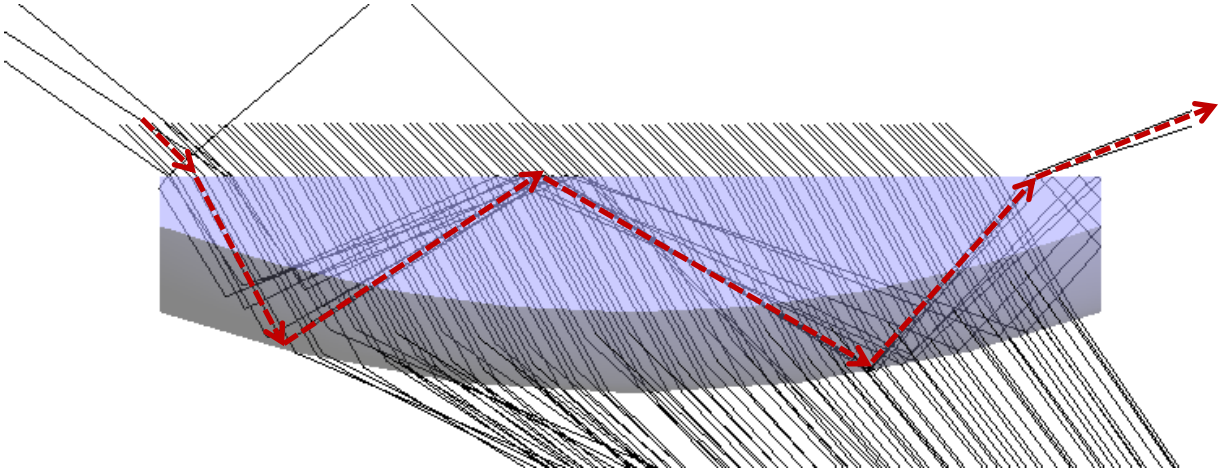

Figure S4: Simulated pathways of light rays at an incidence angle of 45°, one example pathway for the losses due to TIR in the primary lens is highlighted by dashed red lines.

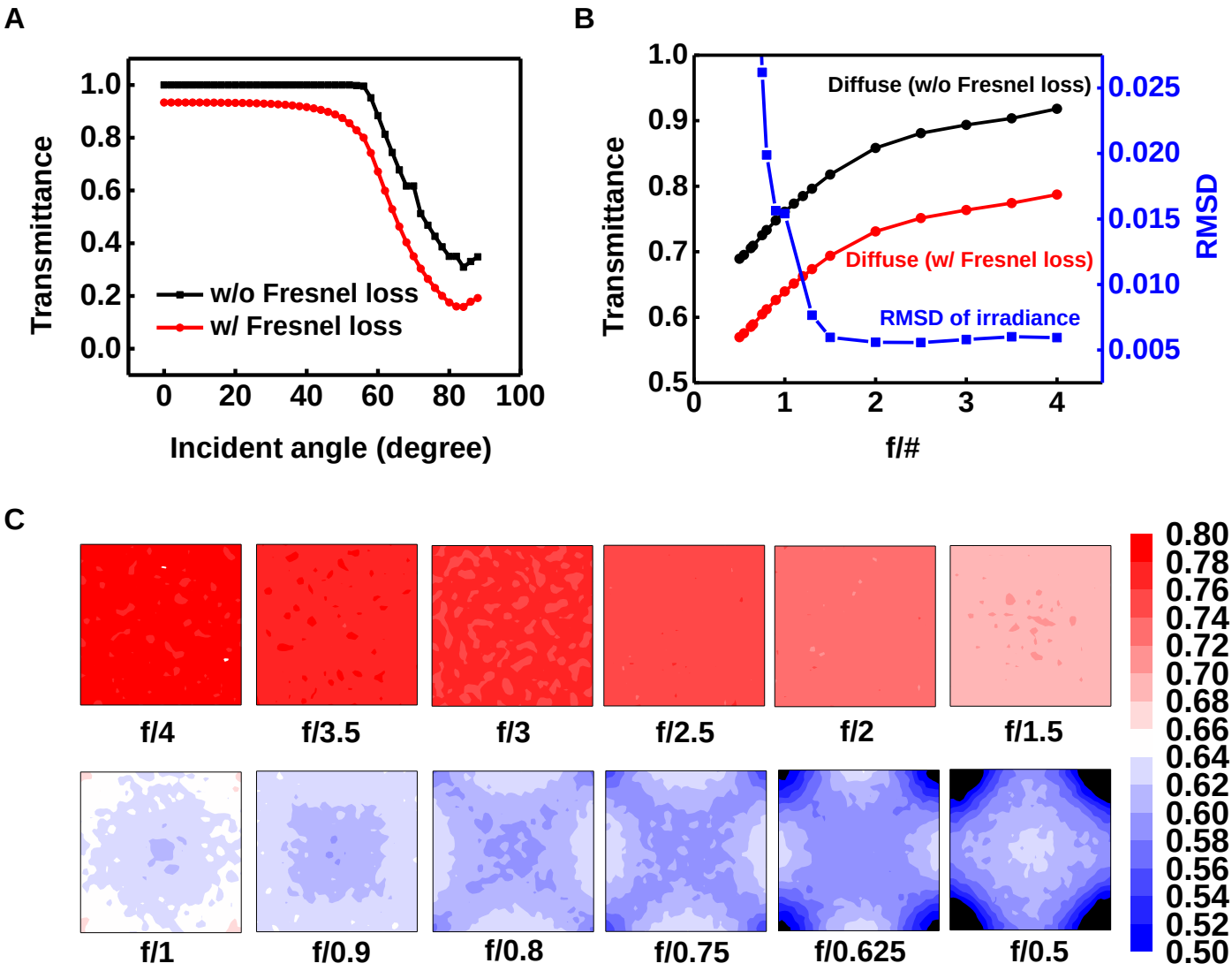

Figure S5: Simulation results for transmittance, irradiance uniformity and irradiance distribution associated with passage of diffuse light (Lambertian) through outward-facing plano-convex lens arrays, similar to the type used in CPV⁺-LP systems. (A) Simulated averaged transmittance of the lens array as a function of the incident angle of light measured relative to the normal direction. (B) Dependence of the transmittance of diffuse/direct sunlight and diffuse irradiance uniformity on the f/# (focal length divided by lens diameter). The calculations involve ray tracing at a wavelength of 550 nm for the case of an infinite lens array, with the lens profile optimized as conic surfaces for convergent focal points. (C) Normalized irradiance distribution under an infinite lens array for different f/#, with a sampling area equivalent to that of a single lens unit: higher f/# leads to a higher irradiance uniformity.

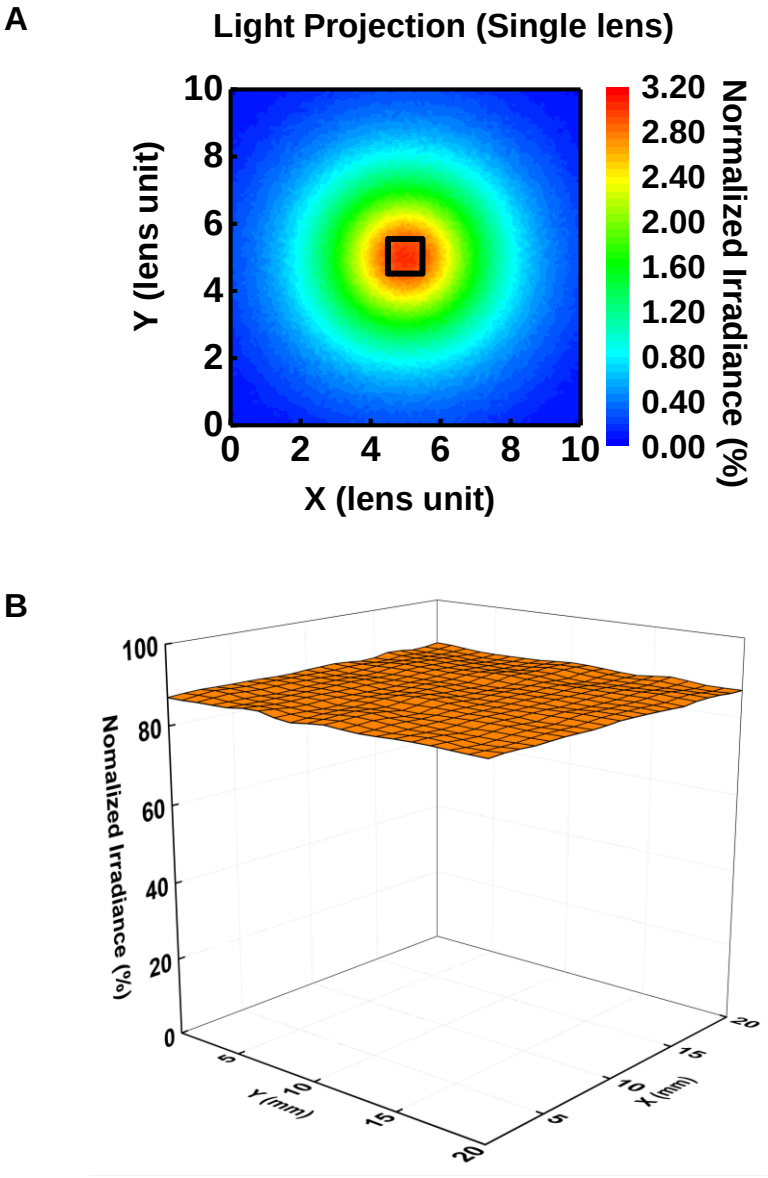

Figure S6: Simulated irradiance distribution of diffuse light projected by (A) a single primary lens unit and (B) an infinite primary lens array. The lens was configured based on the primary lens unit in the HCPV module, with a perfect AR coating (i.e., no Fresnel losses). The angle distribution of the incoming rays in the simulation was assumed to be Lambertian, while their spectral distribution matches the diffuse sunlight in the AM 1.5 diffuse spectrum. The square in the center of (A) illustrates the lens aperture, with a normalized peak irradiance of ~3%, as most rays are projected on areas outside the aperture; in contrast, the normalized irradiance in (B) is much higher (~87%) and more uniform, as a result of the superposition of the single-lens projected irradiance profile.

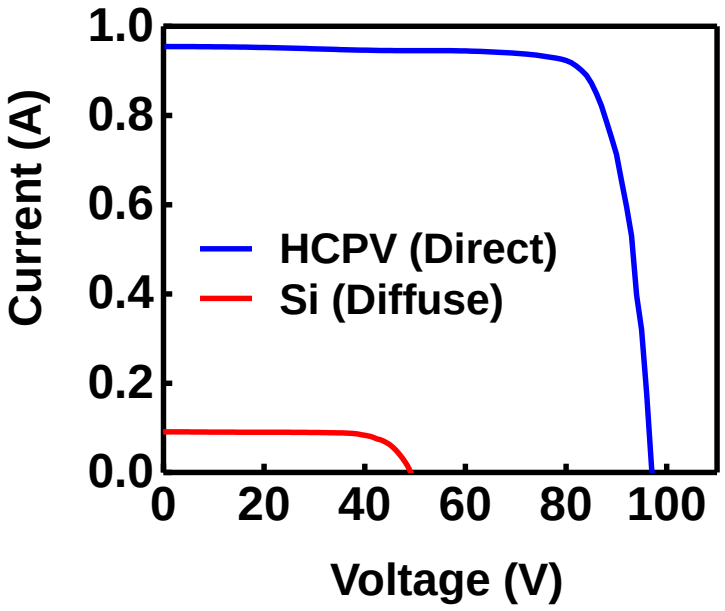

Figure S7: *I-V* curves from the HCPV and Si component of the HCPV^{+} module measured on sun Oct 20, 2015

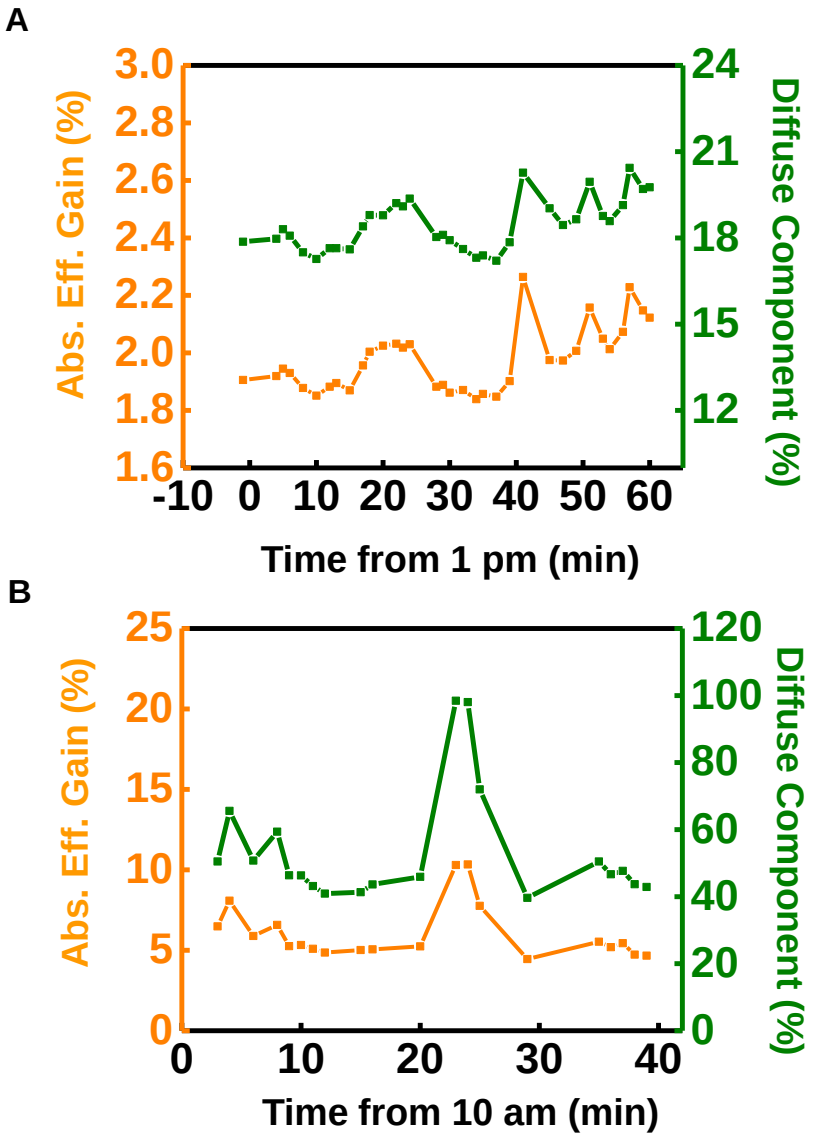

Figure S8: Real-time data of the efficiency gains from Si cells and diffuse components on a (A) sunny day (1.97% enhancement, peaked at 2.2%) and (B) cloudy day (6.06% enhancement, peaked at 10.3%) measured at Bondville, IL on Aug 16th and 31st, 2015 .

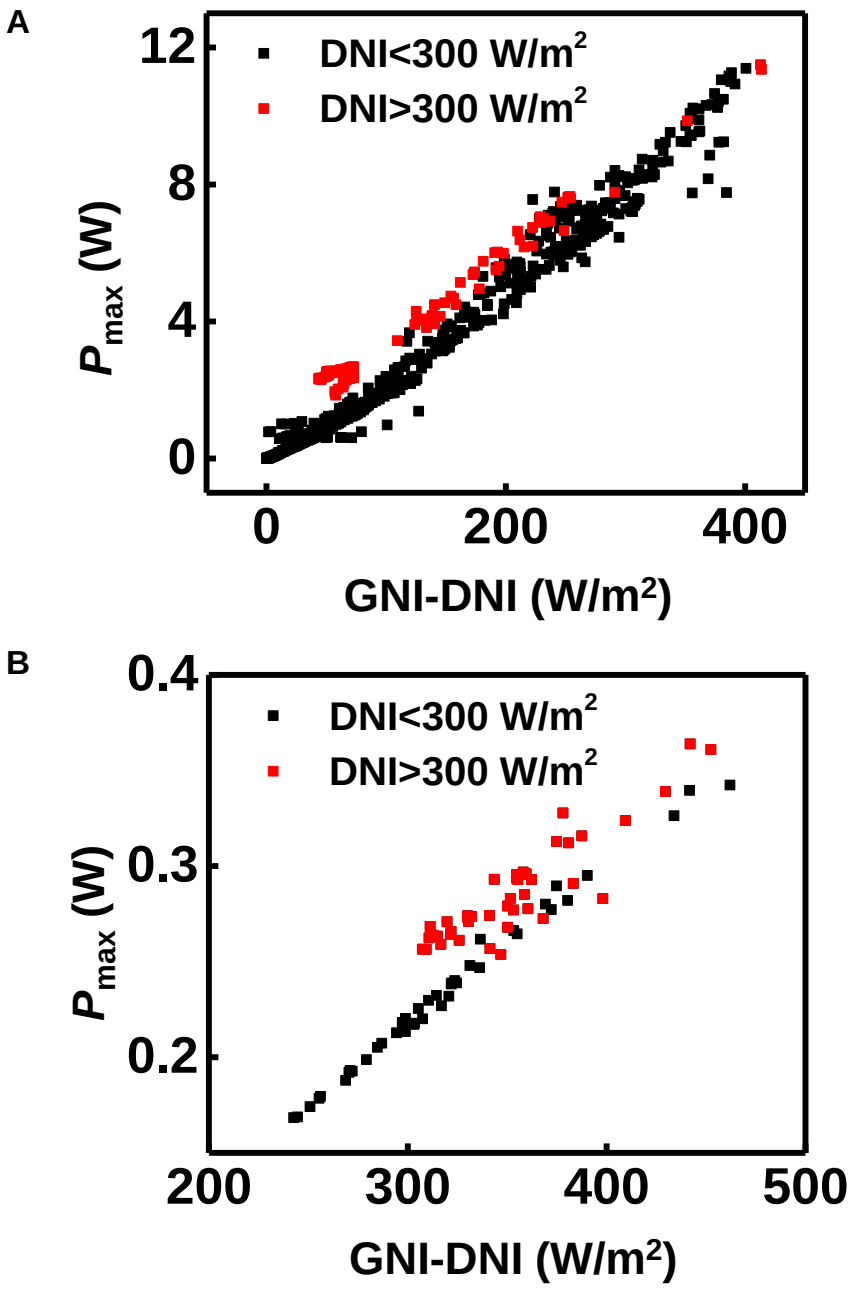

Figure S9: Maximum power generated by Si cells against diffuse solar irradiance (i.e., GNI-DNI) measured for (a) HCPV^{+}-DS module on three different days (Nov 20, Nov 28 and Oct 25, 2015) in Durham, NC; (b) CPV^{+}-LP module on March 3, 2016 in Washington, DC

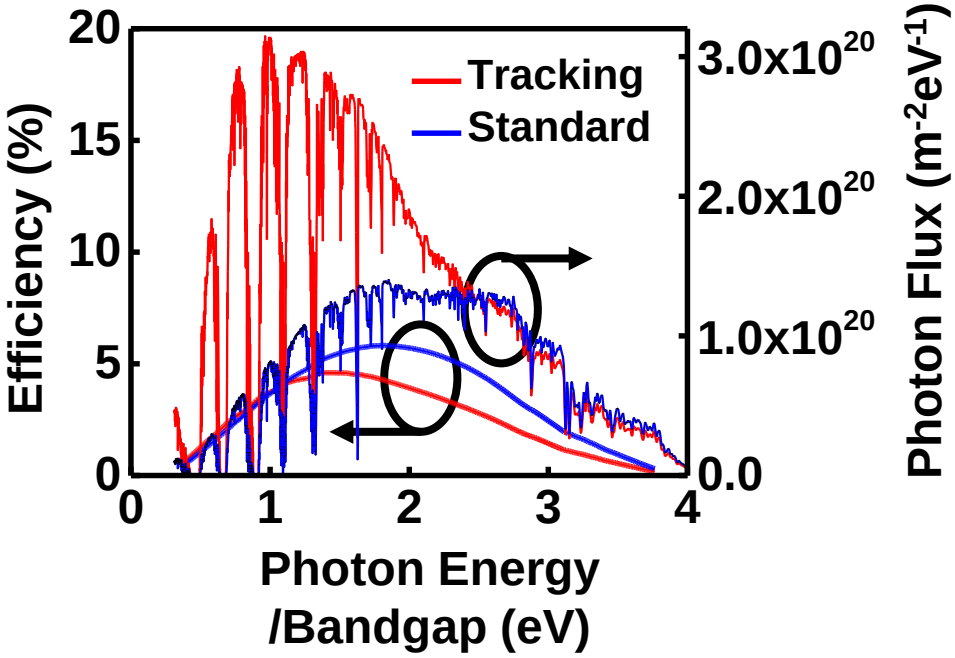

Figure S10: Comparison of diffuse component of standard ASTM G173-03 reference spectrum (AM = 1.5, tilted angle = 37^0, diffuse = tilted global –(tilted direct + circumsolar)) and the corresponding tracking diffuse spectrum (AM=1.5, tilted angle = 48.19^0, diffuse = titled global – titled direct) generated by SMARTS 2.9.5; detailed balance efficiency for both are plotted as well and the optimized bandgap blue-shifted under the standard spectrum. Due to the facts that circumsolar rays can not be fully used by the CPV and the standard spectrum is more suitable for flat plate PV, tracking spectra are used at all AM# for simulations in the main text.

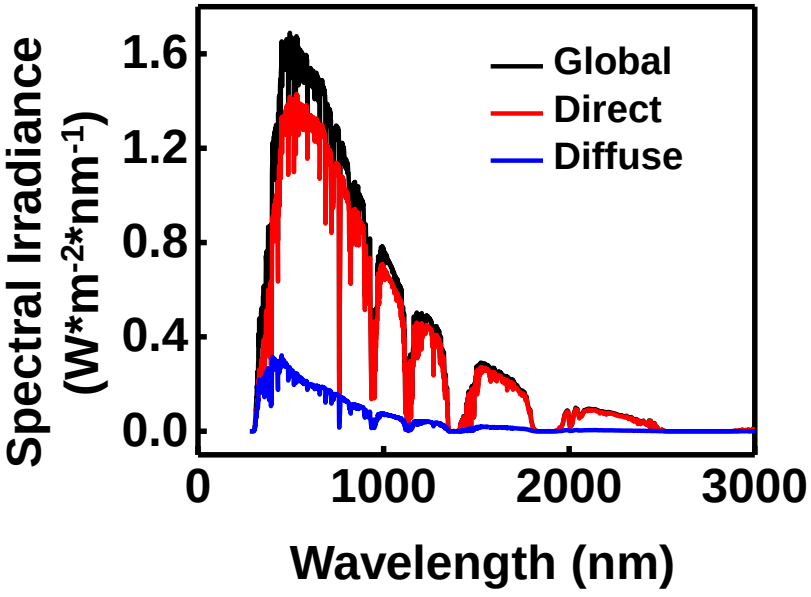

Figure S11: Comparison of the tilted direct, diffuse and global components of the solar spectra at AM=1.5 (tracking), as generated by SMARTS 2.9.5.